Layer by layer coating for bio-functionalization of additively manufactured meta-biomaterials

S. Amin Yavari[a,*,1], M. Croes[a,1], B. Akhavan[b,c,d], F. Jahanmard[a], C.C. Eigenhuis[a], S. Dadbakhsh[e,f], H.C. Vogely[a], M.M. Bilek[b,c,g,h], A.C. Fluit[i], C.H.E. Boel[i], B.C.H. van der Wal[a], T. Vermonden[j], H. Weinans[a,k], A.A. Zadpoor[k]

[a] Department of Orthopedics, University Medical Center Utrecht, Utrecht 3508GA, the Netherlands
[b] School of Aerospace, Mechanical and Mechatronic Engineering, University of Sydney, Sydney, NSW 2006, Australia
[c] School of Physics, University of Sydney, Sydney, NSW 2006, Australia
[d] The Heart Research Institute, 7 Eliza Street, Newtown, Sydney, NSW, 2042 Australia
[e] Department of Production Engineering, KTH Royal Institute of Technology, Brinellvägen 68, SE-10044 Stockholm, Sweden
[f] PMA, Department of Mechanical Engineering, KU Leuven & Member of Flanders Make, Celestijnenlaan 300, B-3001 Leuven, Belgium
[g] Charles Perkins Centre, University of Sydney, Sydney, NSW 2006, Australia
[h] Sydney Nano Institute, University of Sydney, Sydney, NSW 2006, Australia
[i] Department of Medical Microbiology, University Medical Center Utrecht, Utrecht, the Netherlands
[j] Department of Pharmaceutics, Utrecht Institute for Pharmaceutical Sciences (UIPS), Utrecht University, Utrecht 3512JE, the Netherlands
[k] Department of Biomechanical Engineering, Delft University of Technology, Mekelweg 2, Delft 2628CD, the Netherlands

ARTICLE INFO

ABSTRACT

Additive manufacturing has facilitated fabrication of complex and patient-specific metallic meta-biomaterials that offer an unprecedented collection of mechanical, mass transport, and biological properties as well as a fully interconnected porous structure. However, applying meta-biomaterials for addressing unmet clinical needs in orthopedic surgery requires additional surface functionalities that should be induced through tailor-made coatings. Here, we developed multi-functional layer-by-layer coatings to simultaneously prevent implant-associated infections and stimulate bone tissue regeneration. We applied multiple layers of gelatin- and chitosan-based coatings containing either bone morphogenetic protein (BMP)-2 or vancomycin on the surface of selective laser melted porous structures made from commercial pure Titanium (CP Ti) and designed using a triply periodic minimal surface (i.e., sheet gyroid). The additive manufacturing process resulted in a porous structure and met the the design values comparatively. X-ray photoelectron spectroscopy spectra confirmed the presence and composition of the coating layers. The release profiles showed a continued release of both vancomycin and BMP-2 for 2–3 weeks. Furthermore, the developed meta-biomaterials exhibited a very strong antibacterial behavior with up to 8 orders of magnitude reduction in both planktonic and implant-adherent bacteria and no signs of biofilm formation. The osteogenic differentiation of mesenchymal stem cells was enhanced, as shown by two-fold increase in the alkaline phosphatase activity and up to four-fold increase in the mineralization of all experimental groups containing BMP-2. Eight-week subcutaneous implantation in vivo showed no signs of a foreign body response, while connective tissue ingrowth was promoted by the layer-by-layer coating. These results unequivocally confirm the superior multi-functional performance of the developed biomaterials.

1. Introduction

Meta-biomaterials are rationally designed and topologically complex porous structures with rare or unprecedented combinations of mechanical, physical, and biological properties [1–3]. Similar to the other types of designer materials such as mechanical [4–6] and acoustic [7–9] meta-materials, the unusual large-scale properties of meta-biomaterials is a direct consequence of their complex small-scale topological design. This complexity also necessitates the use of free-form fabrication techniques such as additive manufacturing (AM = 3D printing) [10–12].
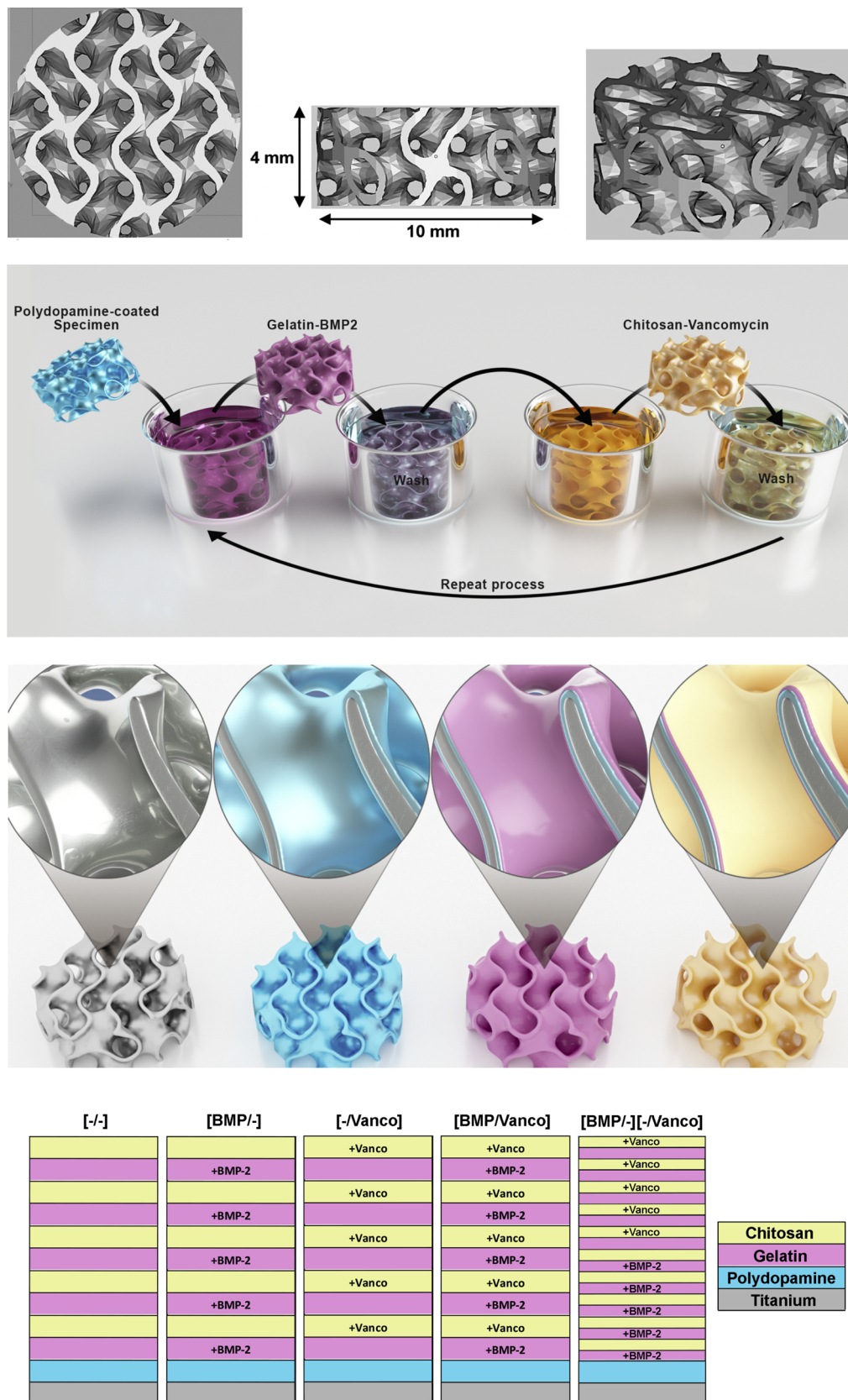
Fig. 1. CAD drawings of the gyroid porous structure used as input for the AM process (a). Schematic illustration of the layer-by-layer coating process (b–c) and the resulting surface layers (d).

Topologically complex biomaterials can be made from a variety of materials, including polymers [13–15] and metals [16–20]. For skeletal applications, however, metals offer unique advantages, including bone-mimicking mechanical properties [21,22], bone-mimicking mass transport properties [23,24], and long fatigue lives [25]. The recent advances in AM techniques have enabled the AM of meta-biomaterials from a wide range of both non-biodegradable [26,27] and biodegradable metals [28,29]. Moreover, the rate of biodegradation of meta-biomaterials is known to be adjustable by topological design [30], particularly because the exposed surface area and the transport of fluid and biodegradation products are highly topology-dependent. All these favorable properties, in conjunction with a fully-interconnected porous structure, are highly beneficial for enhancing the regenerative performance of bone substitutes and for improving the osseointegration of orthopedic implants, as clearly demonstrated in multiple *in vivo* experiments [31–33].

In addition to the above-mentioned topology-related properties, AM meta-biomaterials facilitate the incorporation of additional bio-functionalities by making their hugely increased and highly adjustable surface area available for surface treatments and coatings that could welcome drug delivery agents. Bio-functionalization of meta-biomaterials has, therefore, been used to enhance the osseointegration of meta-biomaterials [34,35] and reduce the rate of bacterial colonizations on implants [36–39]. However, majority of the previous studies have two major limitations. First, they usually offer only a single functionality: either enhanced bone regeneration or antibacterial behavior. Second, the release kinetics provided have not been precisely controlled, making it impossible to achieve complex release profiles that may be required for maximizing the effects of the delivered active agents.

Here, we aimed to develop a new generation of AM metallic meta-biomaterials that 1. exploit the many advantages of such materials, 2. offer multiple functionalities, including enhanced bone regeneration and infection prevention, and 3. allow for creating bespoke release profiles of the active agents. Towards that end, we combined a topological design based on triply periodic minimal surfaces (TPMS) with a layer-by-layer multi-functional coating. AM meta-biomaterials based on TPMS design not only exhibit the above-mentioned favorable properties (*e.g.*, bone mimicking mechanical and transport properties and long fatigue lives [23]) but also possess a zero mean surface curvature, which resembles the curvature of trabecular bone [40]. Given the recent reports that surface curvature regulates tissue regeneration [41–44], TPMS holds great promise for improvement of the bone tissue regeneration performance of AM meta-biomaterials. On the other hand, layer-by-layer (LbL) coatings [45,46] were applied to create customized profiles for the simultaneous release of two types of active agents, namely a growth factor and an antibiotic. The methodology of LbL is based on cyclic immersion of the substrate in oppositely charged polyelectrolyte solutions, leading to the formation of multiple layers on the surface [47]. The adherence of the layers is driven by electrostatic interactions. Different intermolecular interactions have been described, including hydrophobic interactions and covalent bonding [48,49]. An LbL assembly allows for the sequential release of different biomolecules from usually dozens but possibly up to hundreds of consecutive layers [50]. Moreover, the thickness of individual layers formed through the LbL approach can be tuned within a relatively wide range (*i.e.*, between a few nanometers to several micrometers). Finally, LBL assemblies can handle the delivery of drugs and drug carriers ranging in size between proteins and peptides [51] and micrometer-sized drug carriers [52]. The difference in type and concentration of the active agents in each layer, thereby allows for the sequential release of antibiotics to kill any bacteria entering the body peri-operatively and to help the host cells to win the "the race for the surface" [53]. Once the host cells have won the race, growth factors are released to encourage the osteogenic differentiation of mesenchymal stem cells (MSC). Furthermore, multiple sequential layers could be created on top of each other. It is, therefore, possible to realize very complex release profiles. Finally, we used alternating layers of negatively and positively charged polymers to enhance the adhesion of the different layers through electrostatic forces.

2. Materials and methods

2.1. Topological designs and additive manufacturing

A biomimetic topological design satisfying the three design objectives namely a pore size above 300 μm [54], a high surface to volume area and a structure to mimic trabecular bone were used. To meet these criteria, we used a sheet gyroid design, which is defined by the mathematical equation "sin(x). cos(y) + sin(y). cos(z) + sin(z). cos(x) = 0" and was obtained using the 3D surface generator program K3DSurf (http://k3dsurf.sourceforge.net/) (Fig. 1a). The mechanical properties of the current implant design has been extensively studied and reported before [23]. After generating the surfaces, Magics (Materialise, Belgium) was used to generate porous cylinder-shaped parts (in STL format) with diameters of 10 mm and heights of ≈ 4 mm. The sheet thickness of the minimal surfaces was ≈ 370 μm with a pore size (wall distances) of ≈ 1500 μm. These design parameters resulted in a solid volume fraction of 27% (*i.e.*, 73% open porosity) and a total surface area that was ≈ 2.2 times larger than the surface area corresponding to an equally sized solid cylinder. For AM, commercial pure titanium (CP-Ti) powder (grade 1, medical grade quality, LPW, UK) with a particle size in the range of 10 − 45 μm was used. Using this pure Ti powder, the porous parts were fabricated *via* selective laser melting (SLM) technique using a Mlab cusing machine (Concept Laser, Germany). The main features of this SLM equipement were as follow: Continuous (CW) fiber laser of 100 W, laser spot size of 50 μm and a wavelength of 1.06 μm. Also, the process was performed in an inert argon atmosphere with oxygen contamination of below 0.3%. Other production parameters are given in Table 1.

2.2. Morphological characterization

The actual porosity of the implants was also measured using micro-computed tomography (micro-CT; Quantum FX; PerkinElmer, Waltham, US). The scans were made using a field of view of 10 mm and tube settings of 90 kV and 180 mA). The images were converted to the binary format. The ratio of the black pixels to white pixels was used to determine the porosity for each following image. In this way, the porosity could be determined as a function of the height for each specimen. The BoneJ plugin (version 1.4.3) in open-source Fiji software was used to analyze the data [55].

We also measured the porosity of the porous structures through dry weighing of three cylindrical porous Ti samples (diameter ≈ 10 mm, height ≈ 3.8 mm). The total porosity of each specimen, ϕ, was defined by measuring the apparent density, ρ_{app}, using the volume and weight of the specimens and the known solid density of Ti (*i.e.*, $\rho_{bulk} = 4510$ kg/m^3) as $\phi = 1 - \rho_{app}/\rho_{bulk}$.

2.3. Layer-by-layer coating

A layer by layer coating was applied on AM meta-biomaterials

Table 1
Processing parameters used for AM of the porous Ti specimens.

Laser processing parameters	
Laser power, W	42
Scanning velocity, mm/s	180
Hatch spacing, μm	77
Layer thickness, μm	30

Table 2
Specifications of the five different experimental groups evaluated in the current study.

Group	Layers	BMP-2	Vanco	Bilayers
AsM	N/A			
[−/−]	Gel/Chi	–	–	5
[−/Vanco]	Gel/Chi-Vanco	–	0.5 mg/mL	5
[BMP/−]	Gel-BMP-2/Chi	25 µg/mL	–	5
[BMP/Vanco]	Gel-BMP-2/Chi-vanco	25 µg/mL	0.5 mg/mL	5
[BMP/−]/[−/Vanco]	Gel-BMP-2/Chi Gel/Chi-vanco	25 µg/mL	0.5 mg/mL	10

through a multi-step process (Fig. 1b) that resulted in a sequence of layers deposited on top of each other (Fig. 1c). We used chitosan (molecular weight = 300 kDa, degree of deacetylation = 82%, Sigma-Aldrich, Germany) and gelatin (source: porcine skin, Sigma-Aldrich) as the cationic and anionic bases of the coating, respectively. The active agents included BMP-2 (STEMCELL Technologies, Canada) and vancomycin hydrochloride (Sigma-Aldrich). The other materials included anhydrous acetic acid (Sigma-Aldrich), Tris-HCl buffer (1:1, Sigma-Aldrich), and polydopamine powder (Sigma-Aldrich). All reagents were of an analytical grade. Deionized water was used to wash all glassware before use. Except for the as-manufactured (AsM) control group, the specimens belonging to all other groups (Table 2) underwent surface treatment for 24 h in a polydopamine solution containing polydopamine powder (2 mg/mL) in 10 mM Tris-HCl buffer (pH = 8.5). In order to create the layer-by-layer structure of the anionic and cationic polymers on the polydopamine surface-treated specimens, the following steps were followed: preparing gelatin (Gel, 5 mg/mL) in PBS (pH = 5) and chitosan (Chi, 5 mg/mL) in 0.3% acetic acid (pH = 5) solutions to respectively load BMP-2 (25 µg/mL) and vancomycin (0.5 mg/mL) in their carriers, followed by 15 min stirring prior to coating. The coating process included the immersion of the porous Ti disks in Gel/BMP-2 solution (1 mL) for 15 min. Then, the specimens were rinsed with ultrapure water for 5 min. The disks were subsequently immersed in the Chi/Vanco solution (1 mL) and incubated for 15 min, followed by the same rinsing procedure. Finally, the specimens were rinsed for 5 min in 1 mL of ultrapure water and air dried. The same procedures were followed for specimens of the other groups, which ultimately resulted in the active agent loading profiles (Fig. 1d). In short, three additional control groups were created where 5 empty gelatin/chitosan bilayers were loaded (group [-/-]), where BMP-2 was present in the gelatin layers, but the chitosan layers were empty (group [BMP/-]), and where the gelatin layers were empty, but vancomycin was present in the chitosan layers (group [-/Vanco]).While the [BMP/Vanco] group contains both BMP-2 and Vancomycin in their respective layers, the [BMP/−]/[−/Vanco] group does not have the counterpart drug in each bilayer which led to 10 bilayers in total. The latter group was included to have the same amount of drug as the [BMP/Vanco] group, but as such, to provide a more sequential drug release profile. A summary of the specifications of all experimental groups is presented in Table 2.

2.4. Surface characterization

The morphology of the coatings was visualized using a scanning electron microscope (SEM, NovaNano, FEI, US) after gold sputtering for 30 s to make the specimens conductive. In order to choose the representative images of the coated specimens, several regions of the implant surface were quasi-randomly selected for inspection. The inspected locations showed different morphologies of which the images showing some of the recurrent patterns were chosen as the representative images.

The surface chemistry of coatings was analyzed using survey and high-resolution X-ray photoelectron spectroscopy (XPS). The spectra were obtained using a SPECS FlexMod spectrometer (Berlin, Germany) equipped with an MCD9 electron detector and a hemispherical analyzer (PHOIBOS 150). The X-ray monochromatic source (Al Kα, hv = 1486.7 eV) was operated at a power of 200 W (10 kV, 20 mA). The base pressure was always below 5×10^{-8} mbar, and the take-off angle was 90°. High resolution was used to acquire the C1s spectra. High-resolution C1s spectra were compiled using pass energies of 30 and 20 eV and resolutions of 0.5 and 0.1 eV, respectively. Dedicated software (CasaXPS version 2.3.1, producer) was used for the calibration of the spectra, fitting the curves, and calculation of the atomic concentrations.

2.5. In vitro release

The specimens from different groups were submerged in 500 µL PBS (pH = 7.4) and incubated at 37 °C. The PBS was refreshed on days 1, 7, 14, and 28. The concentrations of BMP-2 and vancomycin in the samples at indicated time points were measured to calculate the cumulative release profiles. The concentration of BMP-2 was determined with an enzyme-linked immunosorbent assay (ELISA) kit for human BMP-2 (Peprotech Ltd, London, UK). The concentration of vancomycin was measured through ultra-performance liquid chromatography (UPLC) using an ACQUITY UPLC H-Class PLUS Bio system (Waters Corporation, US) equipped with a BEH C18 Column (1.7 µm, 2.1 mm × 50 mm, Waters). A mobile phase mixture was used consisting of water and acetonitrile, both mixed with 0.1% trifluoroacetic acid. The samples were eluted at a flow rate of 1 mL/min at ambient temperature using a linear gradient elution program of 85% water to 60% acetonitrile. The absorbance was measured at 233 nm using a photodiode array detector (PDA) (Waters 2996, Waters, Canada). Results were analyzed using the software accompanying the PDA detector (Eaters Empower 3 Pro, Waters, Canada).

2.6. Antibacterial assay

A *Staphylococcus aureus* strain (49230, ATCC, US) that is derived from an osteomyelitis patient [56] was used to assess the antibacterial activity of our biomaterials. Specimens (n = 3) from each experimental group were brought in contact with fresh tryptic soy broth (TSB) medium supplemented with 1% bacterial glucose suspension in the mid-log growth phase (OD600 = 0.01, ± 10⁷ bacteria/mL). The container was then kept at 37 °C for 24 h while being continuously stirred atop a shaker. The specimens aimed for the later time points (*i.e.*, 7 and 14 days) were stored in PBS until the day preceding the bacterial quantification (*i.e.*, for 6 and 13 days). The numbers of both planktonic and adherent bacteria were quantified using plate counting of the colony forming units (CFUs) in serial dilutions of the bacterial suspension. In the case of planktonic bacteria, a sample of the incubation medium was taken. As for the adherent bacteria, we first used PBS to rinse the specimens three times before transferring them to fresh PBS and 1 min sonication. The supernatant was used for CFU determination using the same technique as mentioned above.

The samples contaminated with the bacterial suspension were inspected using SEM (JEOL JSM- 6500 F, Japan) after a fixation and dehydration process as detailed below. We used PBS to wash the specimens three times, followed by 2 h of fixation using 2% glutaraldehyde at 4 °C. The dehydration process was performed by immersing each specimen in the following series of solutions, all 5 min per step: 25% ethanol (EtOH), 50% EtOH, 75% EtOH, and 90% EtOH, two times 100% EtOH, 50% EtOH/hexamethyldisilazane, and 100% hexamethyldisilazane. Before SEM inspection, the specimens were dried overnight at room temperature and made conductive by gold sputtering to a thickness of 1 nm.

2.7. MSC isolation and culture

Bone marrow samples were harvested from a total of three patients that underwent orthopedic surgery at the University Medical Center Utrecht (Utrecht, The Netherlands). Written informed consent was given by the patient, after approval of the institutional medical ethics committee. For isolation of MSCs, the mononuclear cell fraction was obtained by Ficoll-Paque centrifugation and cultured for 48 h in growth medium consisting of α-MEM (Invitrogen, CA, USA) supplemented with 100 units/mL Pen Strep antibiotics (Invitrogen), 10% (v/v) Fetal Bovine Serum, and 0.2 mM L-ascorbic acid 2-phosphate (Sigma-Aldrich). The plastic-adherent cells within were expanded to passage 5. The osteogenic differentiation medium (ODM) consisted of normal growth medium containing dexamethasone (10 nM, Sigma-Aldrich) and beta-glycerophosphate (10 mM, Sigma-Aldrich). MSCs were seeded onto the samples in 48 well plates (2×10^5 cells/500 μL) and cultured in a humidified incubator (37 °C, 5% CO_2). The medium was refreshed every fourth day of the culture period.

2.8. Cell viability assays

The cell metabolic activity was quantified over a period of five days following incubation with AlamarBlue Reagent (Thermo Scientific MA, USA). The fluorescence signal was read with a multiplate reader (Fluoroskan Ascent FL, Thermo Labsystems, Helsinki, Finland). The amount of DNA was determined using the Quant-It PicoGreen kit (Invitrogen, CA, USA) following the instructions of the manufacturer. The cell adhesion and survival on the implants after 24 h was assessed using a live & dead cell viability staining (Molecular Probes, Thermo Scientific, MA, USA) as specified by the manufacturer. Samples were imaged on the IX53 fluorescence microscope (Olympus, Tokyo, Japan). Both experiments were performed in triplicate. Calcein (live cell signal) was viewed with a fluorescein bandpass filter, whereas ethidium homodimer (dead cell signal) was viewed with a filter for propidium iodide. Autofluorescence of the Ti discs was excluded by the inclusion of non-cell seeded discs.

2.9. Osteogenic marker expression

All experiments were performed in triplicate. The activity of alkaline phosphatase (ALP) was determined at day 10 in the MSCs cultured in the growth medium. The samples were lysed in 0.2% Triton X-100/PBS for 30 min. A sample was taken to measure the ALP activity according to the conversion of p-nitrophenyl phosphate (pNPP, Sigma FAST pNPP tablets, Sigma-Aldrich). The absorbance values measured at 405/655 nm (Bio-Rad plate reader, CA, US) were normalized to the DNA values measured using the Quant-It PicoGreen kit (Invitrogen).

To assess the amount of calcium deposition, the MSC-seeded specimens were cultured in ODM for 14 days. The specimens were fixated in 4% formaldehyde and stained with 0.2% (w/v) Alizarin Red S (ARS) (pH = 4.2, Sigma-Aldrich) for 60 min. The samples were washed 5×5 min with PBS and subsequently treated with 10% cetylpyridinium (CPC, in 10 mM Na_2PO_4, pH = 7.0) for 30 min on a shaker to remove and measure the amount of bound Alizarin Red S on a microplate reader (Bio-rad) at 595/655 nm. A calibration curve was obtained from a serial dilution of ARS in the CPC buffer. The amount of Ca^{2+} was calculated given that one mole ARS in the solution binds to two moles of Ca^{2+} [57].

Matrix mineralization was visualized after 14 days using a previously published protocol [58]. In short, mineralized nodules were stained by overnight culture in ODM containing 20 μM xylenol orange (XO). The following day, the specimens were fixated in 4% formaldehyde and counterstained for 10 min with 1 μg/mL (w/v) DAPI dihydrochloride (Sigma). The XO signal was then visualized through fluorescence microscopy (IX53, Olympus) using the TRITC Red filter. Autofluorescence of the Ti discs in the DAPI and TRITC Red channels

was excluded by the inclusion of non-cell seeded discs.

2.10. In vivo foreign body response

A rat study was performed with approval of the Ethics Committee for Animal Experimentation of Utrecht University. Permission was received from the Central Authority for Scientific Procedures on Animals under protocol no. AVD115002016445. Five male Fisher rats (F344/IcoCrl, 16-week old, Charles River) were housed at the Central Laboratory Animal Institute (Utrecht University). There were no restrictions on food and water intake.

The rats underwent surgery under anesthesia with 2–3% isoflurane. Pain relief (0.03 mg/kg s.c.; Temgesic®, RB Pharmaceuticals Limited, Slough, UK) was given once pre-operatively and two days post-operatively.

Subcutaneous pocket were made by a skin incision followed by blunt dissection of the subcutaneous tissue. The following groups were implanted into each rat: AsM, [-/-], [BMP/Vanco], [BMP/-][Vanco/-]. The implants were identical to those used in the *in vitro* experiments. The skin was closed with resorbable sutures (Monocryl®, Ethicon, NJ, US). The rats were euthanized with CO_2 after 8 weeks.

2.11. Histology

The explanted Ti discs underwent 4% (w/v) formaldehyde fixation and dehydration in an EtOH series, followed by methyl methacrylate (MMA, Merck Millipore, MA, US) embedding. A 35 μm-thick section was cut from the middle of each sample with a microtome (Leica, Nusslochh, Germany) and stained with methylene blue/basic fuchsin. Subsequently, the percentage of vascularized connective tissue in the available pore space (tissue area%) could be calculated similar to an already published method [59]. In addition, samples were evaluated for the presence of fibrous capsule formation, acute inflammatory cell reaction, and foreign body giant cells.

2.12. Statistical analysis

Data are depicted in the figures as mean ± standard deviation. A one-way ANOVA followed by Tukey *post-hoc* correction was used for comparison of the group means in SPSS (v24, IBM, IL, USA). Statistical analyses were done on the log-transformed CFU data when determining the antibacterial efficiency of the biomaterials.

3. Results

3.1. AM and morphology of the porous biomaterials

After design and slicing, the laser paths were specially designed to only provide non-overlapping contours with distances of 77 μm in order to deliver dense walls close to that of the design file (Fig. 2a). The AM process resulted in porous structures whose morphological characteristics closely matched those of the CAD design (compare Fig. 1a with Fig. 2b). Analysis of the density of the bulk material showed the SLM process has resulted in highly dense material (relative density > 28%). The relative density of the porous structure was within 6.6% of their designed values, indicating a successful application of the AM process (Table 3).

3.2. Surface analysis

The applied coating uniformly covered the surface of the porous specimens with a clear LbL morphology (Fig. 2d-f). Surface elemental composition data (Table 4) showed that carbon and nitrogen atomic concentrations increase upon the deposition of LBL coatings for all samples, and that of oxygen decreases. The Ti atomic concentration decreased from 16.6% for the AsM sample to 0% after the deposition of
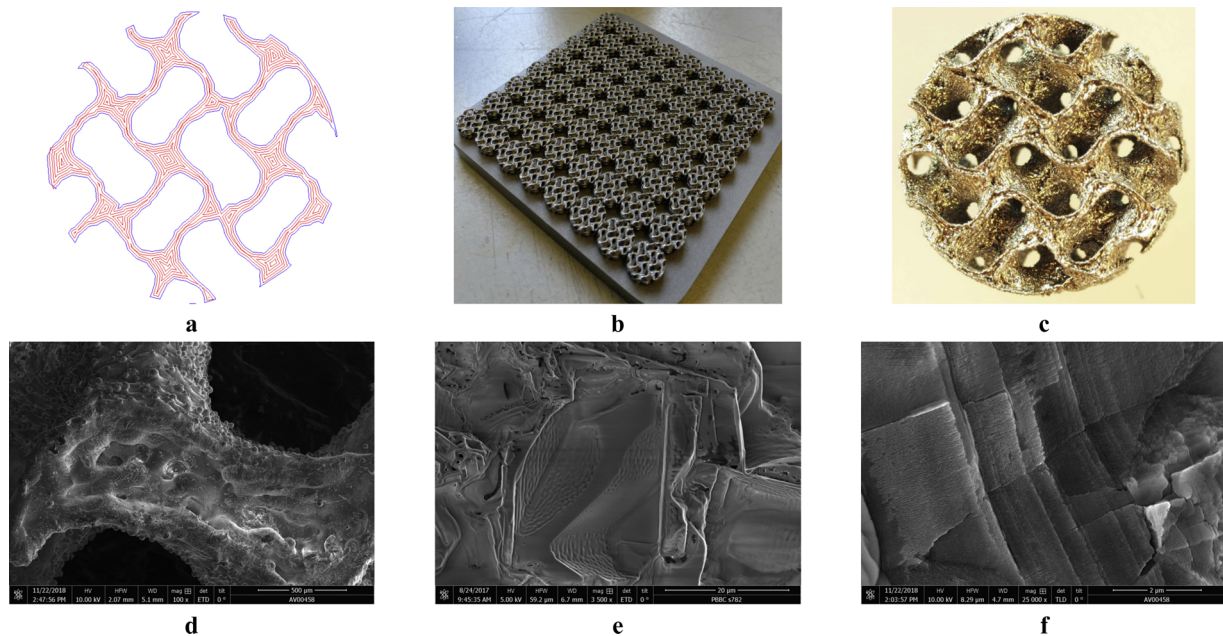
Fig. 2. Hatching and contour slices used for creating the laser scanning paths (a), and the AM porous specimens (b–c). The representative SEM images of the layer-by-layer coating (group [−/−]) (d–f).

Table 3

The porosity measurement of AsM specimens.

	Porosity from micro CT (%)	Porosity from theoretical density (%)
AsM	71 ± 6.2	76 ± 0.2

Table 4

XPS survey elemental composition of uncoated and LbL-coated specimens.

Groups	Atomic concentration (%)				
	Ti	Cl	O	C	N
AsM	16.6	–	51.2	25.5	6.7
[−/−]	–	–	26.7	61.0	12.3
[−/Vanco]	–	0.9	23.2	65.8	10.1
[BMP/−]	–	–	23.3	62.2	14.5
[BMP/Vanco]	–	0.8	23.3	62.4	13.5
[BMP/−]/[−/Vanco]	–	0.9	25.5	63.4	10.2

coatings. The increase of carbon and nitrogen atomic concentrations is due to the formation of LBL layers from gelatin and chitosan that are composed of carbon, nitrogen, and oxygen atoms. The decrease of oxygen and Ti atomic concentrations is due to the formation of sufficiently thick layers of LbL coatings that prevent the escape and detection of core-shell electrons emitted from Ti and the oxygen present in the underlying Ti substrate. The absence of Ti signals confirms that the overall thickness of the LBL coatings for all samples is greater than the sensitivity depth of XPS (8–10 nm) [60]. The surface chemistry of [−/Vanco], [BMP/Vanco], and [BMP/−]/[−/Vanco] specimens showed traces of the Cl structure that is present in the chemical structure of vancomycin, indicating the successful incorporation of this drug into the coatings.

XPS C1s high resolution spectra (Fig. 3a) provided further information on the variations of surface chemistry in the LbL-coated specimens. The carbon spectra were curve fitted with three peaks centered at the binding energies of approximately 284.6, 286.5, and 287.5 eV corresponding to C−C/C−H (C1), C−O/C−N (C2), and C=O/N−C=O (C3) components, respectively [61]. For the group [−/−], the C1 peak arises from C−C/C−H bonds present in gelatin [62], while

peaks C2 and C3 can primarily be assigned to chitosan's carbon atoms bonded to oxygen or to the nitrogen of the amino groups [63]. The inclusion of vancomycin in the [-/Vanco] and [BMP/-]/[-/Vanco] coatings increases the relative concentration of compounds containing C=O/N−C=O groups. These changes in the surface chemistry are explained by the highly oxygenated chemical structure of vancomycin. The inclusion of BMP-2 in the coatings, however, induced less apparent changes in the shape of C1s spectra compared to the vancomycin-containing specimens. Taking into account the thickness of each layer that is estimated to be in the range of 5–10 nm [64], the greater influence of vancomycin on XPS surface chemistry is expected compared to that of BMP-2. Vancomycin is present in chitosan layers including the one on the topmost 5–10 nm of the surface, whereas BMP-2 molecules are loaded into the gelatin layers that sit below the top chitosan layer and, thus, contribute less to the overall XPS signals.

3.3. Release profiles

For all groups containing vancomycin, we detected a burst release in the first day followed by additional release until day 7 (Fig. 3b). The initial burst release was higher for the group with a larger number of bilayers (*i.e.*, [BMP/-]/[-/Vanco]) in comparison with the other groups containing vancomycin (*i.e.*, [BMP/Vanco] and [-/Vanco]) (Fig. 3b). However, the differences leveled off after 7 days with no significant differences detected afterward (Fig. 3b). The release of BMP-2 was faster for the group with 5 coating bilayers (*i.e.*, [BMP/Vanco]) as compared with the group with 10 coating bilayers (*i.e.*, [BMP/-]/[-/Vanco]) (Fig. 3c). The level of the released BMP-2 for the [BMP/-] group, which did not include any vancomycin, was faster than that of the [BMP/-]/[-/Vanco] group (Fig. 3c). A burst release of BMP-2 was detected for all groups, which in the case of the [BMP/-]/[-/Vanco] and [BMP/Vanco] groups was followed by slower release after day 1 (Fig. 3c).

3.4. Antibacterial behavior

At days 1 and 7, the number of both planktonic and adherent bacteria was significantly lower in all groups that contained vancomycin in their coating in comparison with the groups that did not (Fig. 4a-b). The
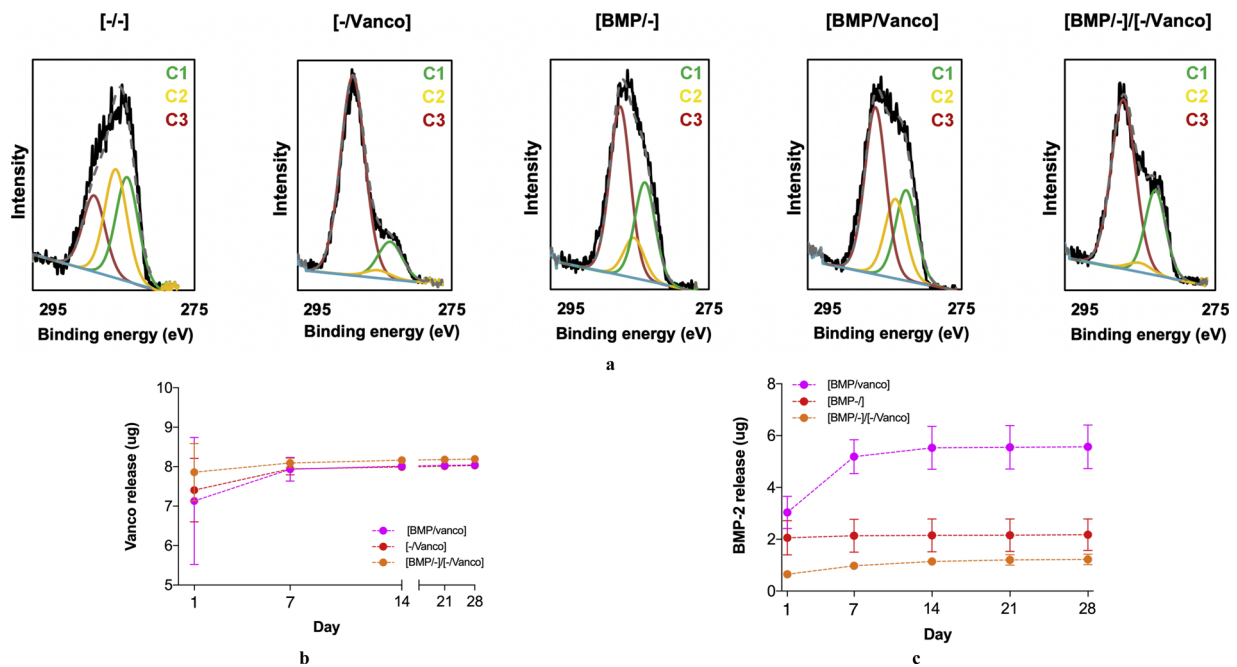
Fig. 3. The XPS spectra corresponding to the different experimental groups (Green: C1, Yellow: C2, Red: C3)(a). Cumulative release profiles of vancomycin (b) and BMP-2 (c) measured by HPLC and BMP-2 ELISA kit, respectively. Data are represented as the mean ± SD (n = 3). (For interpretation of the references to colour in this figure legend, the reader is referred to the web version of this article.)
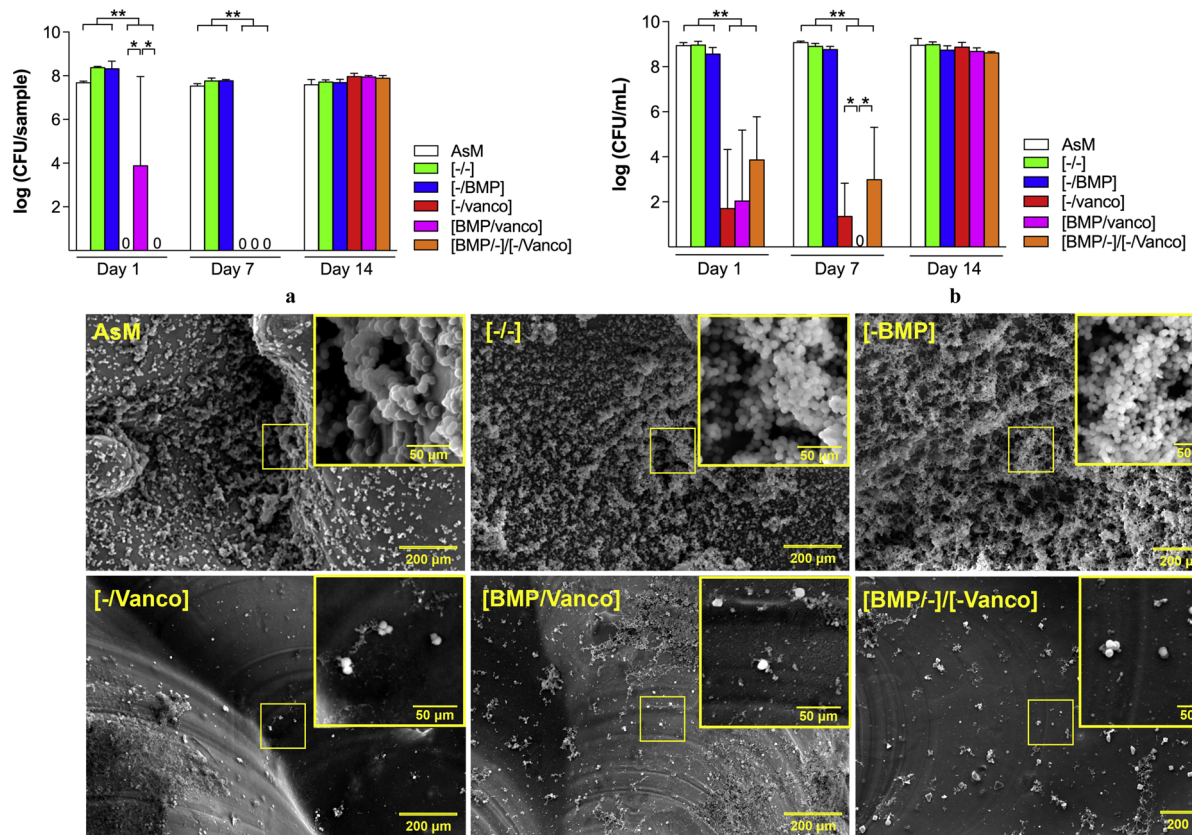

Fig. 4. CFUs of planktonic (a) and adherent (b) bacteria measured for the different experimental groups. Data are represented as the mean ± SD (n = 3). Representative SEM images of the bacteria present on the surface of the specimens from different experimental groups (c–h).

specimens from the [BMP/-]/[-/Vanco] and [-/Vanco] groups resulted in the total eradication of the adherent bacteria at days 1 and 7 (Fig. 4a). The antibacterial effects were diminished by day 14 (Fig. 4a-b). SEM performed on day 1 and confirmed the quantitative CFU assay:

the surface of the specimens from the AsM, [-/-], and [-BMP] groups were associated with multilayer bacterial colony formation (Fig. 4c-e), whereas a limited number of bacteria could be detected in the groups containing vancomycin (Fig. 4f-h).
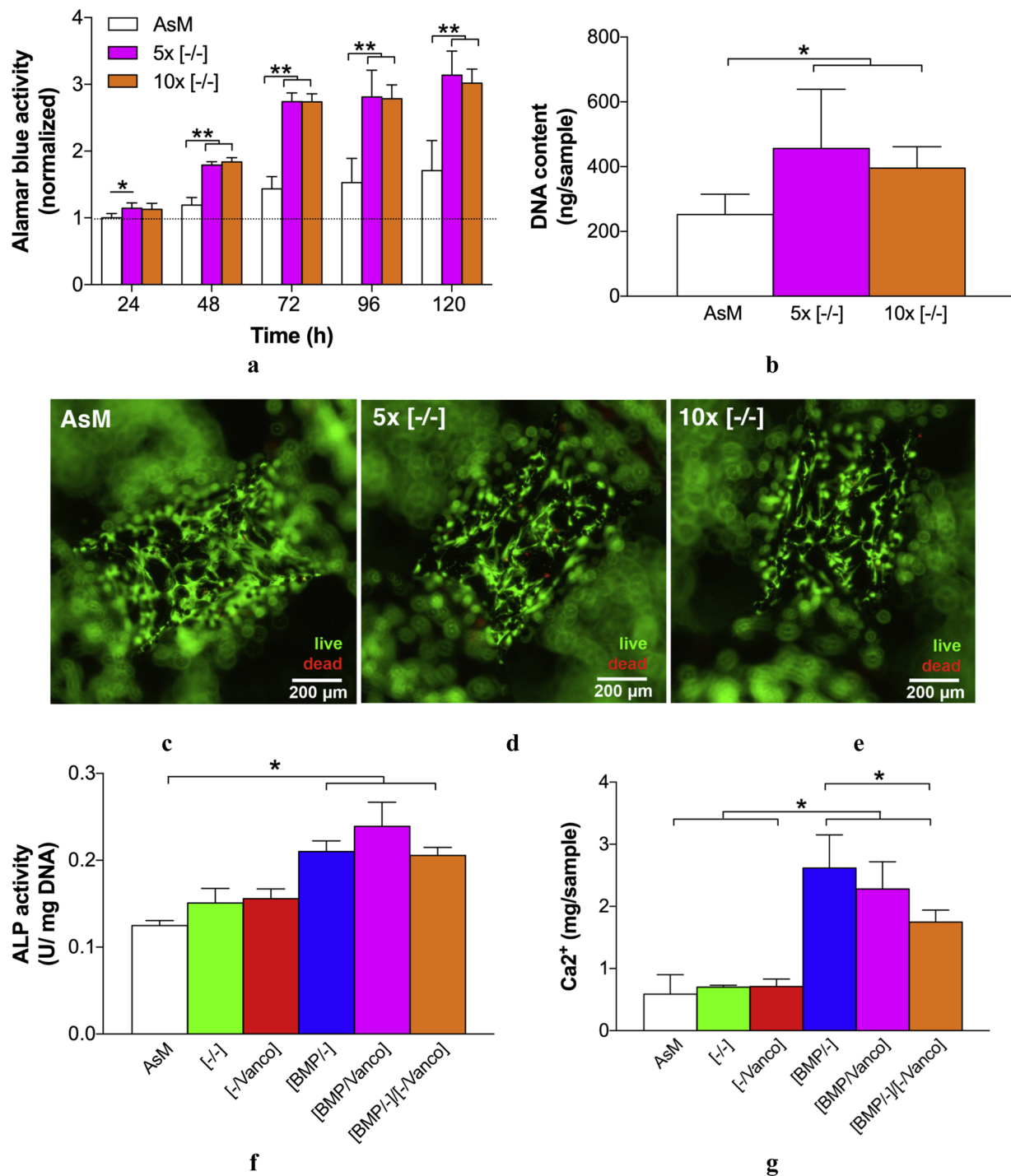
Fig. 5. Alamar blue metabolic activity (a) and Picogreen DNA assays (b) (n = 3 MSC donors, each donor in triplicate) for the AsM group and multiple layers of unloaded gels. Live-dead staining after 24 h shown for specimens from the AsM group (c) as well as 5 (d) and 10 (e) layers of unloaded gels (n = 3 MSC donors, each donor in triplicate). The ALP activity measured for the different experimental groups at day 10 (Picogreen assay)(n = 1 MSC donor in triplicate) (f). Calcium deposition associated with the different experimental groups after 14 days. Data are represented as the mean ± SD. (For interpretation of the references to colour in this figure legend, the reader is referred to the web version of this article.)

3.5. Cytocompatibility and osteogenic differentiation

The live-dead assay showed that surfaces of all the specimens (*i.e.*, specimens from the groups AsM, 5x [-/-], and 10x [-/-]) were equally covered by viable cells (Fig. 5a-c), demonstrating no negative effect of the coatings on cell adhesion and proliferation. Quantitative analyses even showed that, as compared to AsM specimens, both Alamar blue activity and DNA content were significantly higher for 5 and 10 bilayers

of coating (Fig. 5c–e).

The ALP activity in MSCs, measured at day 10, was used as an early marker of osteogenic differentiation (Fig. 5f). An enhanced ALP activity was found in MSCs after culture on implants loaded with BMP-2 coatings. Despite their different BMP-2 release profiles (Fig. 3b–c), there were no apparent differences in the pro-osteogenic effect of BMP-2 coatings with different multilayer build up. For all groups containing BMP-2, we observed a significantly higher ALP activity and a significant
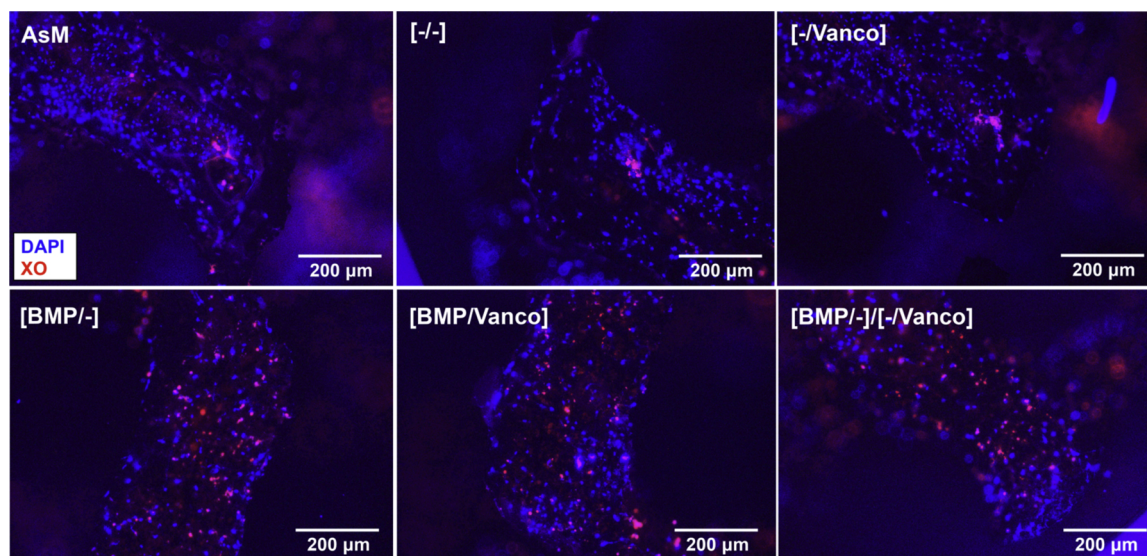
Fig. 6. Calcium deposition in the different experimental groups visualized using Xylenol Orange fluorescent dye (red) together with DAPI nuclear counterstain (blue). Images are representative of the group. (For interpretation of the references to colour in this figure legend, the reader is referred to the web version of this article.)

multi-fold increase in the amount of mineralization as compared to the three other groups that did not contain BMP-2 (Fig. 5f–g).

It was determined whether the drug release from the coatings was sufficiently sustained to promote full osteoblastic differentiation in terms of hMSC matrix mineralization. It was found that all BMP-2-carrying LbL coatings accelerated late osteoblast differentiation, as shown by the higher calcium deposition after 14 days (Fig. 5g). Of the three groups carrying BMP-2, the [BMP/-][-/vanco] group had the least stimulatory effect on MSC mineralization capacity, which is expected given its reduced BMP-2 release (Fig. 3). Staining with the fluorescent dye xylenol orange qualitatively confirmed the enhanced mineralized nodule formation in the groups carrying BMP-2 (Fig. 6a–f).

3.6. Assessment of in vivo foreign body response

The biocompatibility of the samples was assessed after 8-weeks *in vivo* implantation since the presence of foreign body giant cells and fibrous capsule formation at this time point reflects the degree of the foreign body response [65]. The porous Ti structures did not induce an adverse tissue response in any of the groups, shown by the absence of acute inflammation or fibrous encapsulation at the material-tissue interface (Fig. 7a). Vascularized connective tissue ingrowth and fat tissue formation were seen in all groups. In the AsM group, the presence of dead space in the pores indicated that tissue ingrowth had not yet completed in this group. Quantification of the ingrowth of connective tissue demonstrated a significantly higher vascularized tissue formation in the LBL groups as compared to the AsM group (Fig. 7b), which was unaffected by the thickness of the coating or loading with BMP-2/vancomycin. Remnants of the LBL coating were only sporadically seen, suggesting that most of the chitosan and gelatin had degraded by week 8. In the case of any LBL remnants, no acute inflammatory response was seen around the polymer. At the same time, we observed a high density of blood vessel formation (Fig. 7c). Together, these data show the superior *in vivo* biocompatibility of the LBL coated AM porous Ti as compared to the untreated specimens.

4. Discussion

We applied layer-by-layer coatings to AM porous metallic meta-biomaterials with the aim of achieving multi-functional performance, including infection prevention and stimulation of bone tissue ingrowth in orthopedic implants. The *in vitro* and *in vivo* results presented above unequivocally attest to the superior multi-functional behavior of the developed meta-biomaterials including a strong antibacterial behavior, osteogenic stimulatory effects, and high degree of cytocompatibility.

AM meta-biomaterials offer a novel design paradigm within which the various properties of biomaterials could be adjusted using geometrical design, the choice of material, as well as the type and parameters of the applied surface bio-functionalization technique. Recent studies have shown how the above-mentioned design variables could be used to adjust the mechanical properties, mass transport properties, and bio-degradation profiles of AM porous metallic biomaterials and achieve unusual properties that are beneficial for bony ingrowth [66]. However, addressing unmet clinical needs such as the simultaneous prevention of implant-associated infections and stimulation of bone tissue regeneration when treating large bony defects or in immune-compromised patients requires effective delivery of multiple active agents with customized release profiles that befit the application at hand. Up until now, there have been no general design paradigms that allow for the adjustment of the release profiles of multiple active agents. The results of the current study show how layer-by-layer coating can offer such a paradigm to complete the landscape of performance-adjustability in the design of AM porous metallic biomaterials.

4.1. Release profiles and mechanisms

The release of therapeutic agents takes place in two separate ways: 1. diffusion through the multi-layered film and 2. through pieces leaving the film as a result of biodegradation. The kinetics of former depends on the properties of the polymers, the physico-chemical properties of the agent itself, and the strength of the electrostatic interactions, while the latter entirely depends on the biodegradability of the polyelectrolyte multilayers [67]. These two different mechanisms of release provide the possibility to adjust the release kinetics of the delivered therapeutic agents. In order to enhance osseointegration, a sustained presence of osteogenic factors is desirable. When trying to prevent implant-associated infections, however, the therapeutic effect has to be delivered within the first hours or days after implantation. Such an effect is best realized through a burst release of the antibacterial agents. Electrostatic interaction of gelatin/chitosan bilayers may increase the mechanical strength and decrease the inter-diffusion of molecules between layers. Such an effect could explain the reduction of the burst-release of BMP-2 in the [BMP/Vanco] group as compared to simple bilayers. More remarkably, the reduction of the burst-release of
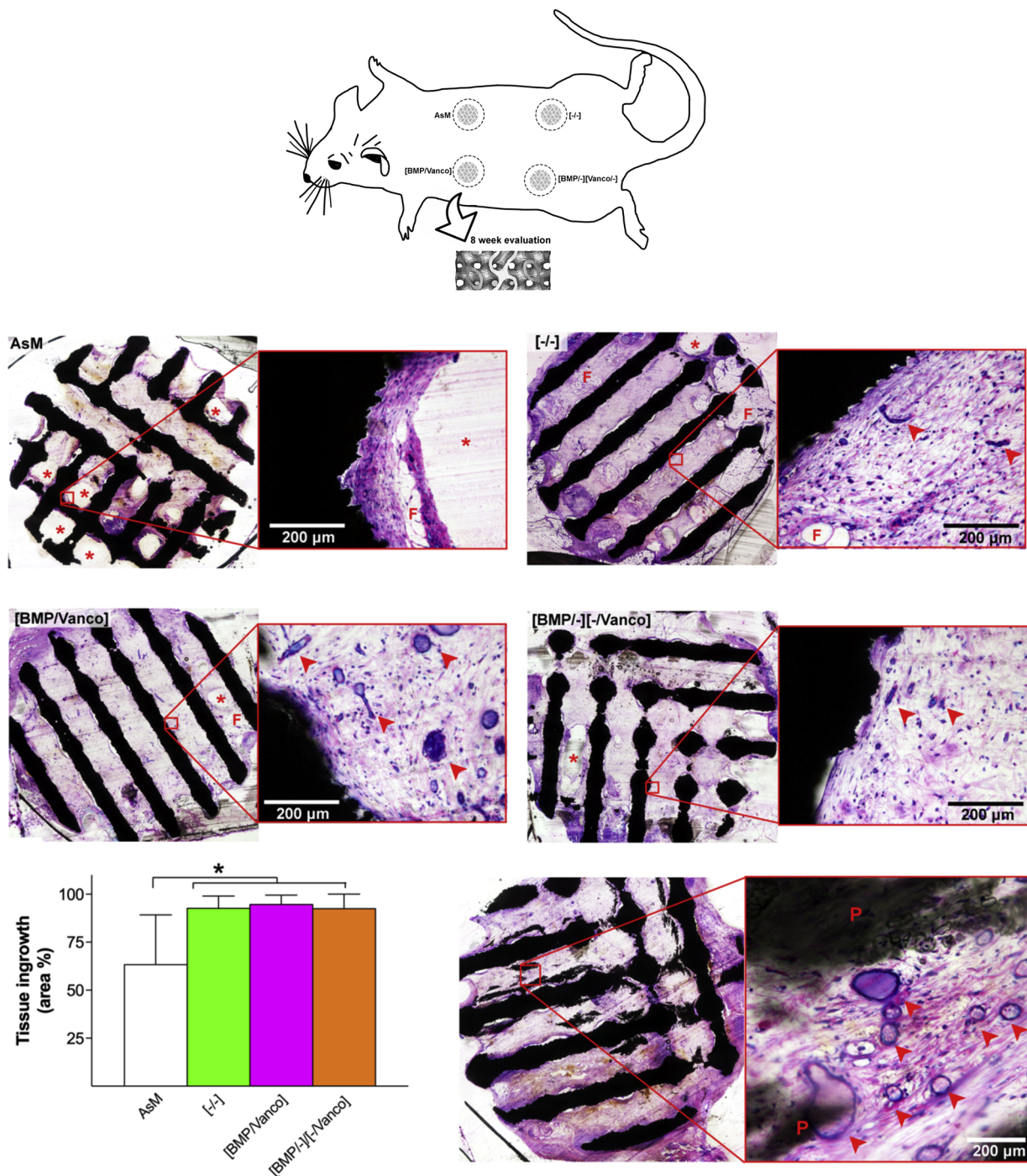
Fig. 7. Methylene blue/basic fuchsin staining to show tissue formation after 8-week subcutaneous implantation in rats (a). Quantification of vascularized connective tissue ingrowth as a percentage of the available pore space (area%) (b). Methylene blue/basic fuchsin staining showing the presence of the remnants of the coating (c). This image of the unloaded-gel group (i.e., [−/−]) is representative of all the experimental groups. Data are represented as the mean ± SD (n = 5 animals). *p < 0.05. Asterisks = dead space; Arrowheads = blood vessel; F = fat tissue; P = polymer. Ti (For interpretation of the references to colour in this figure legend, the reader is referred to the web version of this article.)

BMP-2 in the compartmentalized group [BMP/-][-/vanco] could be explained by the thickness of the coating. In the case of that group, BMP-2 was only incorporated in the 5 lower bilayers, leaving another 5 bilayers on top. On the other hand, the high hydrophilicity of vancomycin gives rise to a higher rate of polymer biodegradation as well as a faster rate of diffusion of the delivered molecules, leading to burst release in all groups [68]. This is in line with our proposed approach to first prevent bacteria colonization and subsequently provide the opportunity for *contact osteogenesis* leading to bone formation at the

implant surface, growing towards the host bone [69].

4.2. The roles of gelatin and chitosan

In the current study, gelatin and chitosan were deemed the ideal candidates for the LBL coating, as they will ionically interact to form a polyion complex given their opposite charges. Chitosan additionally has antibacterial effects, which can help to further reduce the risk of implant-associated infections [38,70]. Here, we clearly demonstrated that

gelatin/chitosan gels, in addition to their excellent properties for tunable drug delivery, might also offer improved biocompatibility to Ti implants. Titanium by itself is a relatively bioinert material, and a hydrogel layer can offer improved bioactivity and better integration with bone tissue [71]. *In vitro*, we found that the gelatin/chitosan coating promoted the proliferation of MSCs, which is in accordance with other reports [72]. In line with this finding, we observed *in vivo* that the gelatin/chitosan coating accelerated vascularized connective ingrowth as compared to non-coated Ti implants. In the literature, mixed results have been reported for chitosan and gelatin in terms of their effects on cell proliferation or angiogenesis. First, incorporation of gelatin into chitosan coatings yields a better attachment and spreading of osteoblasts in comparison to the use of chitosan alone [73]. Second, there are numerous reports in support of the several antiangiogenic effects of chitosan [74,75]. Taken together, the current evidence points to the fact that a synergistic interaction between gelatin and chitosan forms the basis of the improved biocompatibility. Although this requires further investigation, it has been speculated that the specific electrostatic interaction of gelatin and chitosan decreases the net surface charge of the coatings, which subsequently improves the hydrogel-cell interaction [73].

4.3. The potential of LbL coatings

A layer-by-layer coating offers the possibility to achieve what is usually very difficult to realize in the local delivery of active agents, namely sequential delivery of multiple molecules with pre-planned release profiles. Every layer selectively targets a biological response through the active agents it contains. Moreover, the thickness, as well as the biodegradation rate of the different layers, could be designed to allow for the implementation of time delays. This combination of design variables, at least in theory, allows for an step-wise approximation of a number of release profiles. AM meta-biomaterials with multi-functional layer-by-layer coatings can, therefore, reach an unprecedented level of tunability in their properties and, thus, functionalities. This constitutes a worthwhile addition to the growing trend of "designer biomaterials" [76,77].

Given the fact that the different functionalities of biomaterials may require very different timelines, it may be even impossible to achieve proper multi-functionality unless sequential delivery can be programmed into the design of the meta-biomaterials. In the specific case of the biomaterials developed here where the dual functionalities include infection prevention and the stimulation of the osteogenic differentiation of MSCs, the initial release of vancomycin is essential to kill the bacteria entering the wound peri-operatively and to assist the host cells in winning the "race for the surface". Once the host cells have populated the surface of the porous implant, the release of BMP-2 helps in the differentiation of MSCs towards the osteogenic lineage and, thus, *de novo* bone formation. The process of cell migration required for reaching the MSCs to populate the internal surfaces of the porous structure means that the delayed release of BMP-2 may be beneficial for imparting the maximum osteogenic effect. Moreover, alternating between the release of both types of molecules allows for creating an on-off effect, which is desirable in a host of biomaterial applications (*e.g.*, see [78–80]). Similar to our approach, other researchers have also exploited the potential of LbL coatings to enhance the bone regeneration performance of bone implants [81,82].

Another time-related aspect in the design of infection-prevention coatings is the risk of antibacterial resistance that arises when bacteria are exposed to low concentrations of antibiotics (*i.e.*, concentrations below minimum inhibitory concentrations, MIC) for a prolonged period of time. Given the fact that the antibiotic reservoir of all coatings depletes over time, all permanent coatings delivering antibiotics will eventually start to locally deliver sub-MIC concentrations of antibiotics, which may not be desirable. The *in vitro* release profiles measured for the coatings developed here show that the cumulative release leveled

off after 3 weeks. Moreover, *in vivo* observations verified that the coating was almost fully degraded after 8 weeks. Given the fact that the risk of peri-operative infections is present only in the first few weeks after surgery, biodegradation after that period of time guarantees that the high doses of antibiotics are released within the most critical period after surgery. This strategy assists the host cells in winning the race for the surface and to prevent the formation of biofilms (Fig. 4c-h), while minimizing the risk of the development of antibiotic resistance resulting from prolonged exposure to sub-MIC doses of antibiotics. There will, of course, be no additional protection against long-term infections that may occur either hematogenously or contiguously [83]. To create such protections, separate mechanisms would be needed.

4.4. Limitations and future work

In this study, we focused on performing a wide range of *in vitro* and *in vivo* assays that were used to evaluate the performance of the LbL coatings in terms of improving the bone tissue regeneration performance and inducing a strong antibacterial behavior. All of the performed assays supported the favorable performance of the applied coatings. Whether or not the observed favorable performance is a direct consequence of a "precisely controlled release kinetics" cannot, however, be determined solely based on the data presented here. It is, therefore, suggested that future studies should evaluate the mechanistic aspects of such LbL coatings to establish the relationship between the release kinetics realized through layer-by-layer coatings and the readouts from *in vitro* and *in vivo* assays.

This proof-of-concept study, nevertheless, paves the way for further exploration of the possibilities offered by meta-biomaterials and the advantages that LbL coatings offer such as fine-tuning the therapeutic release pattern and using stimuli-responsive layers through further coating optimization and *in vivo* studies. The main limitations of the study, therefore, relate to the above-mentioned directions that still need to be explored. In particular, there is a need for a systematic study of how LbL coatings could be used to obtain arbitrarily complex release profiles of multiple active agents. Moreover, the *in vivo* evaluation performed here was limited to the assessment of the biocompatibility and safety of the applied LbL coatings. More extensive *in vivo* experiments using infection and bone regeneration animal models are required to study the *in vivo* performance of the developed meta-biomaterials in preventing implant-associated infections and improving bone tissue regeneration performance of AM metallic meta-biomaterials.

5. Conclusions

We developed AM porous metallic meta-biomaterials with multi-functional layer-by-layer coatings that have the potential to prevent implant-associated infections and stimulate bone tissue regeneration through enhanced osteogenic differentiation of MSCs. The developed biomaterials exhibited a very strong antibacterial response with up to 8 orders of magnitude reduction in the number of both planktonic and adherent bacteria and no biofilm formation. In terms of osteogenic activity, the groups containing BMP-2 exhibited significantly enhanced ALP activity and a multi-fold increase in mineralization. *In vivo*, we did not detect any foreign body response, including no adverse tissue response, while there was substantial growth of connective tissue. Together, these results confirm the superior multi-functional performance of the developed meta-biomaterials. This combination of favorable mechanical properties, a fully interconnected porous structure, protection against implant-associated infections, and enhanced bone tissue regeneration response make the developed biomaterials a promising candidate for the development of a new generation of orthopedic implants.

Declaration of Competing Interest

The authors declare that there is no conflict of interest.

Acknowledgments

References

[1] S. Amin Yavari, S.M. Ahmadi, R. Wauthle, B. Pouran, J. Schrooten, H. Weinans, A.A. Zadpoor, Relationship between unit cell type and porosity and the fatigue behavior of selective laser melted meta-biomaterials, J. Mech. Behav. Biomed. Mater. 43 (2015) 91–100.

[2] H.M. Kolken, S. Janbaz, S.M. Leeflang, K. Lietaert, H.H. Weinans, A.A. Zadpoor, Rationally designed meta-implants: a combination of auxetic and conventional meta-biomaterials, Mater. Horiz. 5 (1) (2018) 28–35.

[3] A.A. Zadpoor, Mechanical performance of additively manufactured meta-biomaterials, Acta Biomater. 85 (2019) 41–59.

[4] J. Berger, H. Wadley, R. McMeeking, Mechanical metamaterials at the theoretical limit of isotropic elastic stiffness, Nature 543 (7646) (2017) 533.

[5] J.H. Lee, J.P. Singer, E.L. Thomas, Micro-/nanostructured mechanical metamaterials, Adv. Mater. 24 (36) (2012) 4782–4810.

[6] X. Zheng, H. Lee, T.H. Weisgraber, M. Shusteff, J. DeOtte, E.B. Duoss, J.D. Kuntz, M.M. Biener, Q. Ge, J.A. Jackson, Ultralight, ultrastiff mechanical metamaterials, Science 344 (6190) (2014) 1373–1377.

[7] S.A. Cummer, J. Christensen, A. Alù, Controlling sound with acoustic metamaterials, Nat. Rev. Mater. 1 (3) (2016) 16001.

[8] J. Mei, G. Ma, M. Yang, Z. Yang, W. Wen, P. Sheng, Dark acoustic metamaterials as super absorbers for low-frequency sound, Nat. Commun. 3 (2012) 756.

[9] L. Zigoneanu, B.-I. Popa, S.A. Cummer, Three-dimensional broadband omnidirectional acoustic ground cloak, Nat. Mater. 13 (4) (2014) 352.

[10] S.C. Ligon, R. Liska, Jr. Stampfl, M. Gurr, R. Mülhaupt, Polymers for 3D printing and customized additive manufacturing, Chem. Rev. 117 (15) (2017) 10212–10290.

[11] M. Salmi, J. Tuomi, K.-S. Paloheimo, R. Björkstrand, M. Paloheimo, J. Salo, R. Kontio, K. Mesimäki, A.A. Mäkitie, Patient-specific reconstruction with 3D modeling and DMLS additive manufacturing, Rapid Prototyp. J. 18 (3) (2012) 209–214.

[12] X. Wang, S. Xu, S. Zhou, W. Xu, M. Leary, P. Choong, M. Qian, M. Brandt, Y.M. Xie, Topological design and additive manufacturing of porous metals for bone scaffolds and orthopaedic implants: a review, Biomaterials 83 (2016) 127–141.

[13] B. Gao, Q. Yang, X. Zhao, G. Jin, Y. Ma, F. Xu, 4D Bioprinting for Biomedical Applications, Trends Biotechnol. 34 (9) (2016) 746–756.

[14] F.P. Melchels, M.A. Domingos, T.J. Klein, J. Malda, P.J. Bartolo, D.W. Hutmacher, Additive manufacturing of tissues and organs, Prog. Polym. Sci. 37 (8) (2012) 1079–1104.

[15] S. Miao, N. Castro, M. Nowicki, L. Xia, H. Cui, X. Zhou, W. Zhu, S.J. Lee, K. Sarkar, G. Vozzi, Y. Tabata, J. Fisher, L.G. Zhang, 4D printing of polymeric materials for tissue and organ regeneration, Mater. Today 20 (10) (2017) 577–591.

[16] C. Han, Y. Li, Q. Wang, S. Wen, Q. Wei, C. Yan, L. Hao, J. Liu, Y. Shi, Continuous functionally graded porous titanium scaffolds manufactured by selective laser melting for bone implants, J. Mech. Behav. Biomed. Mater. 80 (2018) 119–127.

[17] Y. Kajima, A. Takaichi, T. Nakamoto, T. Kimura, Y. Yogo, M. Ashida, H. Doi, N. Nomura, H. Takahashi, T. Hanawa, Fatigue strength of Co–Cr–Mo alloy clasps prepared by selective laser melting, J. Mech. Behav. Biomed. Mater. 59 (2016) 446–458.

[18] C.Y. Lin, T. Wirtz, F. LaMarca, S.J. Hollister, Structural and mechanical evaluations of a topology optimized titanium interbody fusion cage fabricated by selective laser melting process, J. Biomed. Mater. Res. A 83 (2) (2007) 272–279.

[19] P. Lipinski, A. Barbas, A.-S. Bonnet, Fatigue behavior of thin-walled grade 2 titanium samples processed by selective laser melting, Application to life prediction of porous titanium implants, Journal of the Mechanical Behavior of Biomedical Materials 28 (2013) 274–290.

[20] B. Van Hooreweder, Y. Apers, K. Lietaert, J.-P. Kruth, Improving the fatigue performance of porous metallic biomaterials produced by Selective Laser Melting, Acta Biomater. 47 (2017) 193–202.

[21] A.A. Zadpoor, R. Hedayati, Analytical relationships for prediction of the mechanical properties of additively manufactured porous biomaterials, J. Biomed. Mater. Res. A. 104 (12) (2016) 3164–3174.

[22] S. Amin Yavari, R. Wauthle, J. van der Stok, A.C. Riemslag, M. Janssen, M. Mulier, J.P. Kruth, J. Schrooten, H. Weinans, A.A. Zadpoor, Fatigue behavior of porous biomaterials manufactured using selective laser melting, Mater. Sci. Eng. C 33 (8) (2013) 4849–4858.

[23] F. Bobbert, K. Lietaert, A.A. Eftekhari, B. Pouran, S. Ahmadi, H. Weinans, A. Zadpoor, Additively manufactured metallic porous biomaterials based on minimal surfaces: A unique combination of topological, mechanical, and mass transport properties, Acta Biomater. 53 (2017) 572–584.

[24] S. Truscello, G. Kerckhofs, S. Van Bael, G. Pyka, J. Schrooten, H. Van Oosterwyck, Prediction of permeability of regular scaffolds for skeletal tissue engineering: a combined computational and experimental study, Acta Biomater. 8 (4) (2012) 1648–1658.

[25] R. Wauthle, J. Van Der Stok, S.A. Yavari, J. Van Humbeeck, J.-P. Kruth, A.A. Zadpoor, H. Weinans, M. Mulier, J. Schrooten, Additively manufactured porous tantalum implants, Acta Biomater. 14 (2015) 217–225.

[26] Z. Gorgin Karaji, M. Speirs, S. Dadbakhsh, J.-P. Kruth, H. Weinans, A. Zadpoor, S. Amin Yavari, Additively manufactured and surface biofunctionalized porous nitinol, ACS Appl. Mater. Interfaces 9 (2) (2017) 1293–1304.

[27] S.A. Amin Yavari, R. Wauthle, A.J. Bottger, J. Schrooten, H. Weinans, A.A. Zadpoor, Crystal structure and nanotopographical features on the surface of heat-treated and anodized porous titanium biomaterials produced using selective laser melting, Appl. Surf. Sci. 290 (2014) 287–294.

[28] C. Shuai, B. Wang, Y. Yang, S. Peng, C. Gao, 3D honeycomb nanostructure-encapsulated magnesium alloys with superior corrosion resistance and mechanical properties, Compos. Part B Eng. 162 (2019) 611–620.

[29] C. Shuai, Y. Cheng, Y. Yang, S. Peng, W. Yang, F. Qi, Laser additive manufacturing of Zn-2Al part for bone repair: formability, microstructure and properties, J. Alloys. Compd. 798 (2019) 606–615.

[30] Y. Li, H. Jahr, P. Pavanram, F.S.L. Bobbert, U. Puggi, X.Y. Zhang, B. Pouran, M.A. Leeflang, H. Weinans, J. Zhou, A.A. Zadpoor, Additively manufactured functionally graded biodegradable porous iron, Acta Biomater. 96 (2019) 646–661.

[31] N. Reznikov, O.R. Boughton, S. Ghouse, A.E. Weston, L. Collinson, G.W. Blunn, J.R. Jeffers, J.P. Cobb, M.M. Stevens, Individual response variations in scaffold-guided bone regeneration are determined by independent strain-and injury-induced mechanisms, Biomaterials 194 (2019) 183–194.

[32] N. Taniguchi, S. Fujibayashi, M. Takemoto, K. Sasaki, B. Otsuki, T. Nakamura, T. Matsushita, T. Kokubo, S. Matsuda, Effect of pore size on bone ingrowth into porous titanium implants fabricated by additive manufacturing: an in vivo experiment, Mater. Sci. Eng. C 59 (2016) 690–701.

[33] S. Amin Yavari, J. van der Stok, Y.C. Chai, R. Wauthle, Z.T. Birgani, P. Habibovic, M. Mulier, J. Schrooten, H. Weinans, A.A. Zadpoor, Bone regeneration performance of surface-treated porous titanium, Biomaterials 35 (24) (2014) 6172–6181.

[34] J. Van der Stok, M. Koolen, M. De Maat, S. Amin Yavari, J. Alblas, P. Patka, J. Verhaar, E. Van Lieshout, A.A. Zadpoor, H. Weinans, Full regeneration of segmental bone defects using porous titanium implants loaded with BMP-2 containing fibrin gels, Eur. Cell. Mater. 2015 (29) (2015) 141–154.

[35] J. Van Der Stok, D. Lozano, Y.C. Chai, S. Amin Yavari, A.P. Bastidas Coral, J.A. Verhaar, E. Gómez-Barrena, J. Schrooten, H. Jahr, A.A. Zadpoor, Osteostatin-coated porous titanium can improve early bone regeneration of cortical bone defects in rats, Tissue Eng. Part A 21 (9-10) (2015) 1495–1506.

[36] S. Amin Yavari, L. Loozen, F.L. Paganelli, S. Bakhshandeh, K. Lietaert, J.A. Groot, A.C. Fluit, C. Boel, J. Alblas, H.C. Vogely, Antibacterial behavior of additively manufactured porous titanium with nanotubular surfaces releasing silver ions, ACS Appl. Mater. Interfaces 8 (27) (2016) 17080–17089.

[37] S. Bakhshandeh, Z. Gorgin Karaji, K. Lietaert, A.C. Fluit, C.E. Boel, H.C. Vogely, T. Vermonden, W.E. Hennink, H. Weinans, A.A. Zadpoor, S. Amin Yavari, Simultaneous Delivery of Multiple Antibacterial Agents from Additively Manufactured Porous Biomaterials to Fully Eradicate Planktonic and Adherent Staphylococcus aureus, ACS Appl. Mater. Interfaces 9 (31) (2017) 25691–25699.

[38] M. Croes, S. Bakhshandeh, I. van Hengel, K. Lietaert, K. van Kessel, B. Pouran, B. van der Wal, H. Vogely, W. Van Hecke, A. Fluit, C.E. Boel, J. Albas, A.A. Zadpoor, H. Weinans, S. Amin Yavari, Antibacterial and immunogenic behavior of silver coatings on additively manufactured porous titanium, Acta Biomater. 81 (2018) 315–327.

[39] I.A. Van Hengel, M. Riool, L.E. Fratila-Apachitei, J. Witte-Bouma, E. Farrell, A.A. Zadpoor, S.A. Zaat, I. Apachitei, Selective laser melting porous metallic implants with immobilized silver nanoparticles kill and prevent biofilm formation by methicillin-resistant Staphylococcus aureus, Biomaterials 140 (2017) 1–15.

[40] H. Jinnai, Y. Nishikawa, M. Ito, S.D. Smith, D.A. Agard, R.J. Spontak, Topological similarity of sponge-like bicontinuous morphologies differing in length scale, Adv. Mater. 14 (22) (2002) 1615–1618.

[41] L. Pieuchot, J. Marteau, A. Guignandon, T. Dos Santos, I. Brigaud, P.-F. Chauvy, T. Cloatre, A. Ponche, T. Petithory, P. Rougerie, Curvotaxis directs cell migration through cell-scale curvature landscapes, Nat. Commun. 9 (1) (2018) 3995.

[42] J.R. Vetsch, R. Müller, S. Hofmann, The influence of curvature on three-dimensional mineralized matrix formation under static and perfused conditions: an in vitro bioreactor model, J. R. Soc. Interface 13 (123) (2016) 20160425.

[43] M. Werner, S.B. Blanquer, S.P. Haimi, G. Korus, J.W. Dunlop, G.N. Duda, D.W. Grijpma, A. Petersen, Surface curvature differentially regulates stem cell migration and differentiation via altered attachment morphology and nuclear deformation, Adv. Sci. 4 (2) (2017) 1600347.

[44] M. Werner, N.A. Kurniawan, G. Korus, C.V. Bouten, A. Petersen, Mesoscale substrate curvature overrules nanoscale contact guidance to direct bone marrow stromal cell migration, J. R. Soc. Interface 15 (145) (2018) 20180162.

[45] J. Min, K.Y. Choi, E.C. Dreaden, R.F. Padera, R.D. Braatz, M. Spector, P.T. Hammond, Designer dual therapy nanolayered implant coatings eradicate biofilms and accelerate bone tissue repair, ACS Nano 10 (4) (2016) 4441–4450.

[46] J.J. Richardson, M. Björnmalm, F. Caruso, Technology-driven layer-by-layer assembly of nanofilms, Science 348 (6233) (2015) aaa2491.

[47] G. Decher, Fuzzy Nanoassemblies: Toward Layered Polymeric Multicomposites, Science 277 (5330) (1997) 1232–1237.

[48] J.M. Silva, R.L. Reis, J.F. Mano, Biomimetic extracellular environment based on natural origin polyelectrolyte multilayers, Small 12 (32) (2016) 4308–4342.

[49] F.-X. Xiao, M. Pagliaro, Y.-J. Xu, B. Liu, Layer-by-layer assembly of versatile nanoarchitectures with diverse dimensionality: a new perspective for rational

construction of multilayer assemblies, Chem. Soc. Rev. 45 (11) (2016) 3088–3121.

[50] J.H. Ryu, P.B. Messersmith, H. Lee, Polydopamine surface chemistry: a decade of discovery, ACS Appl. Mater. Interfaces 10 (9) (2018) 7523–7540.

[51] M.M. de Villiers, D.P. Otto, S.J. Strydom, Y.M. Lvov, Introduction to nanocoatings produced by layer-by-layer (LbL) self-assembly, Adv. Drug Deliv. Rev. 63 (9) (2011) 701–715.

[52] X. Qiu, S. Leporatti, E. Donath, H. Möhwald, Studies on the drug release properties of polysaccharide multilayers encapsulated ibuprofen microparticles, Langmuir 17 (17) (2001) 5375–5380.

[53] H.J. Busscher, H.C. van der Mei, G. Subbiahdoss, P.C. Jutte, J.J. van den Dungen, S.A. Zaat, M.J. Schultz, D.W. Grainger, Biomaterial-associated infection: locating the finish line in the race for the surface, Sci. Transl. Med. 4 (153) (2012) 153rv10-153rv10.

[54] V. Karageorgiou, D. Kaplan, Porosity of 3D biomaterial scaffolds and osteogenesis, Biomaterials 26 (27) (2005) 5474–5491.

[55] J. Schindelin, I. Arganda-Carreras, E. Frise, V. Kaynig, M. Longair, T. Pietzsch, S. Preibisch, C. Rueden, S. Saalfeld, B. Schmid, Fiji: an open-source platform for biological-image analysis, Nat. Methods 9 (7) (2012) 676.

[56] M. Lucke, G. Schmidmaier, S. Sadoni, B. Wildemann, R. Schiller, A. Stemberger, N. Haas, M. Raschke, A new model of implant-related osteomyelitis in rats, Journal of Biomedical Materials Research Part B: Applied Biomaterials: An Official Journal of The Society for Biomaterials, The Japanese Society for Biomaterials, and The Australian Society for Biomaterials and the Korean Society for Biomaterials 67 (1) (2003) 593–602.

[57] C.M. Stanford, P.A. Jacobson, E.D. Eanes, L.A. Lembke, R.J. Midura, Rapidly forming apatitic mineral in an osteoblastic cell line (UMR 10601 BSP), J. Biol. Chem. 270 (16) (1995) 9420–9428.

[58] Y.H. Wang, Y. Liu, P. Maye, D.W. Rowe, Examination of mineralized nodule formation in living osteoblastic cultures using fluorescent dyes, Biotechnol. Prog. 22 (6) (2006) 1697–1701.

[59] M. Croes, M. Kruyt, W. Groen, K. Van Dorenmalen, W. Dhert, F. Öner, J. Alblas, Interleukin 17 enhances bone morphogenetic protein-2-induced ectopic bone formation, Sci. Rep. 8 (1) (2018) 7269.

[60] L.J. Martin, B. Akhavan, M.M.M. Bilek, Electric fields control the orientation of peptides irreversibly immobilized on radical-functionalized surfaces, Nat. Commun. 9 (1) (2018) 357.

[61] B. Akhavan, S.G. Wise, M.M.M. Bilek, Substrate-regulated growth of plasma-polymerized films on carbide-forming metals, Langmuir 32 (42) (2016) 10835–10843.

[62] X. Yu, P. Yang, M.G. Moloney, L. Wang, J. Xu, Y. Wang, L. Liu, Y. Pan, Electrospun Gelatin Membrane Cross-Linked by a Bis (diarylcarbene) for Oil/Water Separation: A New Strategy To Prepare Porous Organic Polymers, ACS Omega 3 (4) (2018) 3928–3935.

[63] H. Maachou, M.J. Genet, D. Aliouche, C.C. Dupont-Gillain, P.G. Rouxhet, XPS analysis of chitosan–hydroxyapatite biomaterials: from elements to compounds, Surf. Interface Anal. 45 (7) (2013) 1088–1097.

[64] J.M. Silva, J.R. García, R.L. Reis, A.J. García, J.F. Mano, Tuning cell adhesive properties via layer-by-layer assembly of chitosan and alginate, Acta Biomater. 51 (2017) 279–293.

[65] J.M. Anderson, A. Rodriguez, D.T. Chang, Foreign Body Reaction to Biomaterials, Seminars in Immunology, Elsevier, 2008, pp. 86–100.

[66] A.A. Zadpoor, Additively manufactured porous metallic biomaterials, J. Mater.

Chem. B (2019).

[67] L. Séon, P. Lavalle, P. Schaaf, F. Boulmedais, Polyelectrolyte multilayers: a versatile tool for preparing antimicrobial coatings, Langmuir 31 (47) (2015) 12856–12872.

[68] D. Juric, N.A. Rohner, H.A. von Recum, Molecular Imprinting of Cyclodextrin Supramolecular Hydrogels Improves Drug Loading and Delivery, Macromol. Biosci. 19 (1) (2019) 1800246.

[69] J.E. Davies, Bone bonding at natural and biomaterial surfaces, Biomaterials 28 (34) (2007) 5058–5067.

[70] D. Raafat, K. Von Bargen, A. Haas, H.-G. Sahl, Insights into the mode of action of chitosan as an antibacterial compound, Appl. Environ. Microbiol. 74 (12) (2008) 3764–3773.

[71] H. Cheng, K. Yue, M. Kazemzadeh-Narbat, Y. Liu, A. Khalilpour, B. Li, Y.S. Zhang, N. Annabi, A. Khademhosseini, Mussel-Inspired Multifunctional Hydrogel Coating for Prevention of Infections and Enhanced Osteogenesis, ACS Appl. Mater. Interfaces 9 (13) (2017) 11428–11439.

[72] K. Cai, A. Rechtenbach, J. Hao, J. Bossert, K.D. Jandt, Polysaccharide-protein surface modification of titanium via a layer-by-layer technique: characterization and cell behaviour aspects, Biomaterials 26 (30) (2005) 5960–5971.

[73] T. Jiang, Z. Zhang, Y. Zhou, Y. Liu, Z. Wang, H. Tong, X. Shen, Y. Wang, Surface functionalization of titanium with chitosan/gelatin via electrophoretic deposition: characterization and cell behavior, Biomacromolecules 11 (5) (2010) 1254–1260.

[74] R. Ahmadi, A.J. Burns, J.D. de Bruijn, Chitosan-based hydrogels do not induce angiogenesis, J. Tissue Eng. Regen. Med. 4 (4) (2010) 309–315.

[75] K.H. Prashanth, R. Tharanathan, Depolymerized products of chitosan as potent inhibitors of tumor-induced angiogenesis, Biochim. Biophys. Acta 1722 (1) (2005) 22–29.

[76] N. Doshi, S. Mitragotri, Designer biomaterials for nanomedicine, Adv. Funct. Mater. 19 (24) (2009) 3843–3854.

[77] L. Li, J. Eyckmans, C.S. Chen, Designer biomaterials for mechanobiology, Nat. Mater. 16 (12) (2017) 1164.

[78] M. Amoli-Diva, R. Sadighi-Bonabi, K. Pourghazi, Switchable on/off drug release from gold nanoparticles-grafted dual light-and temperature-responsive hydrogel for controlled drug delivery, Mater. Sci. Eng. C 76 (2017) 242–248.

[79] Q. Gan, J. Zhu, Y. Yuan, H. Liu, J. Qian, Y. Li, C. Liu, A dual-delivery system of pH-responsive chitosan-functionalized mesoporous silica nanoparticles bearing BMP-2 and dexamethasone for enhanced bone regeneration, J. Mater. Chem. B 3 (10) (2015) 2056–2066.

[80] P.T. Hammond, Building biomedical materials layer-by-layer, Mater. Today 15 (5) (2012) 196–206.

[81] G. Cheng, C. Yin, H. Tu, S. Jiang, Q. Wang, X. Zhou, X. Xing, C. Xie, X. Shi, Y. Du, H. Deng, Z. Li, Controlled Co-delivery of growth factors through layer-by-Layer assembly of core–Shell nanofibers for improving bone regeneration, ACS Nano 13 (6) (2019) 6372–6382.

[82] Z. Jia, P. Xiu, S.-I. Roohani-Esfahani, H. Zreiqat, P. Xiong, W. Zhou, J. Yan, Y. Cheng, Y. Zheng, Triple-Bioinspired Burying/Crosslinking Interfacial Coassembly Strategy for Layer-by-Layer Construction of Robust Functional Bioceramic Self-Coatings for Osteointegration Applications, ACS Appl. Mater. Interfaces 11 (4) (2019) 4447–4469.

[83] A. Trampuz, A.F. Widmer, Infections associated with orthopedic implants, Curr. Opin. Infect. Dis. 19 (4) (2006) 349–356.